# Tunable Mechanical Response of Self-Assembled Nanoparticle Superlattices

Somayajulu Dhulipala,[†] Daryl W. Yee,[‡] Ziran Zhou,[¶] Rachel Sun,[†] José E. Andrade,[¶] Robert J. Macfarlane,[‡] and Carlos M. Portela[*,†]

[†]*Department of Mechanical Engineering, Massachusetts Institute of Technology, Cambridge, Massachusetts, USA - 02139*

[‡]*Department of Material Science and Engineering, Massachusetts Institute of Technology, Cambridge, Massachusetts, USA - 02139*

[¶]*Department of Mechanical and Civil Engineering, California Institute of Technology, Pasadena, California, USA - 91125*

E-mail: cportela@mit.edu

Phone: +1 617 715 2680

**Abstract**

Self-assembled nanoparticle superlattices (NPSL) are an emergent class of self-architected nanocomposite materials that possess promising properties arising from precise nanoparticle ordering. Their multiple coupled properties make them desirable as functional components in devices where mechanical robustness is critical. However, questions remain about NPSL mechanical properties and how shaping them affects their mechanical response. Here, we perform *in situ* nanomechanical experiments that evidence up to an black eleven-fold increase in stiffness (black ∼1.49 to 16.9 GPa) and black five-fold increase in strength (black ∼88 to 426 MPa) because of surface stiffening/strengthening from shaping these nanomaterials via focused-ion-beam milling. To

predict the mechanical properties of shaped NPSLs, we present discrete element method (DEM) simulations and an analytical core-shell model that capture the FIB-induced stiffening response. This work presents a route for tunable mechanical responses of self-architected NPSLs, and provides two frameworks to predict their mechanical response and guide the design of future NPSL-containing devices.

**Keywords:** nanoparticle superlattices, self-architected materials, in situ nanomechanics, surface stiffening, FIB shaping

Nanoparticle superlattices (NPSLs), a type of nanocomposite material system composed of ordered arrays of nanoparticles, have demonstrated unique properties that arise from the ordering of their nanoparticle building blocks.[1] By tailoring the compositions of the inorganic nanoparticle core, the organic ligands on their surface, and the superlattice crystal symmetry, NPSLs constitute a family of nanocomposites that can be architected to exhibit enhanced and/or emergent plasmonic,[2–4] photonic,[5–7] magnetic,[8,9] and catalytic[10,11] properties. Owing to their multiple tunable parameters as well as their self-assembled nature, NPSLs represent one of the most versatile types of nano-architected materials, surpassing other emerging material systems such as truss-based nanolattices[12] in terms of minimum feature size and fabrication yield. As a result, significant interest exists in using NPSLs to develop new technologies or novel devices. However, there are still key challenges facing their adoption, such as the lack of processing methods to shape these NPSLs[1] as well as understanding of their process-property relations, especially in the mechanical realm.[13]

Current state-of-the-art syntheses of NPSLs often result in either two-dimensional (2D) thin films,[14–18] polycrystalline aggregates with no defined 3D geometry, or in single crystals with thermodynamically defined 3D shapes,[3,19–24] which limit their utility in combination with other materials or as device elements. Consequently, a variety of top-down additive[25–27] or subtractive[28,29] methods have been developed to shape these self-assembled nanocomposites into form factors that could broaden their end-use cases. In particular, focused ion

beam (FIB) micro/nanomilling, a technique used extensively in the semiconductor industry to make 3D nanostructures and devices,[30,31] has shown potential for shaping NPSLs into functional microscopic devices black as waveguides,[32] fresnel lenses for optical applications,[33] and magnonic metamaterials for microwave antenna applications.[34] Despite this progress, questions remain about the impact of the FIB milling process on the mechanical properties of the NPSLs, which is critical for their subsequent processing and integration into devices.

While a growing number of studies have focused on characterizing the mechanical properties of NPSLs,[35–38] the impact of patterning and shaping them remains unclear. Furthermore, most studies on the mechanical behavior of NPSLs have largely been conducted using *ex situ* nanoindentation[36,38–43] and atomic force microscopy,[37,44,45] which limit observation of material behavior during deformation and under controlled stress states. Although measurement techniques such as *in situ* compression[46] or *in situ* X-ray scattering[47] can be used to obtain a holistic understanding of the mechanical behavior of polycrystalline NPSLs, fundamental questions about the response of single crystals remain.

Here, we use *in situ* uniaxial compression on FIB-milled substrate-bound single-crystal NPSLs to quantify the effect of shaping on their mechanical response. Through nanomechanical experiments conducted concurrently with scanning electron microscopy (SEM), we systematically determine the effective stiffness and strength of the NPSLs, and we uncover order-of-magnitude increases in their mechanical properties stemming from surface stiffening effects. In addition, we provide analytical and numerical predictive tools, in the form of a core-shell composite model and discrete element method (DEM) simulations, respectively, to enable the design of NPSL-based architectures as components in devices.

To obtain consistent mechanical properties of NPSLs under uniaxial compression, it is necessary to examine single-crystal structures that have a uniform cross-sectional area along the axis of compression. Therefore, we opted to examine single-crystal NPSLs assembled via heterogeneous nucleation from a substrate, often referred to as Winterbottom (WB) constructions.[48,49 23,50] In particular, previous work by the authors has shown that face-

centered cubic (FCC) WB NPSLs form flat hexagonal platelets that have minimal variation in their cross-sectional area, making them ideal for mechanical analysis.[23] WB NPSLs were synthesized using nanocomposite tectons (NCTs)[51–54] and assembled via thymine (Thy)-melamine interactions[55](Fig. 1a), as described in the Supporting Information.

SEM imaging of the substrate revealed substrate-bound faceted NCT assemblies that adopted the flat hexagonal platelet shape consistent with that of FCC WB constructions[23] (Fig. 1b). Further, FIB-milled internal cross-sections of the NPSLs, indicated that the nanoparticles were arranged in a close-packed configuration (Fig. 1c), as expected for an FCC crystal structure. As validation, fast Fourier transform (FFT) analysis of the SEM cross-sectional images (Fig. 1c, inset) produced arcs with 6-fold symmetry, which is consistent with ordering of an FCC structure.

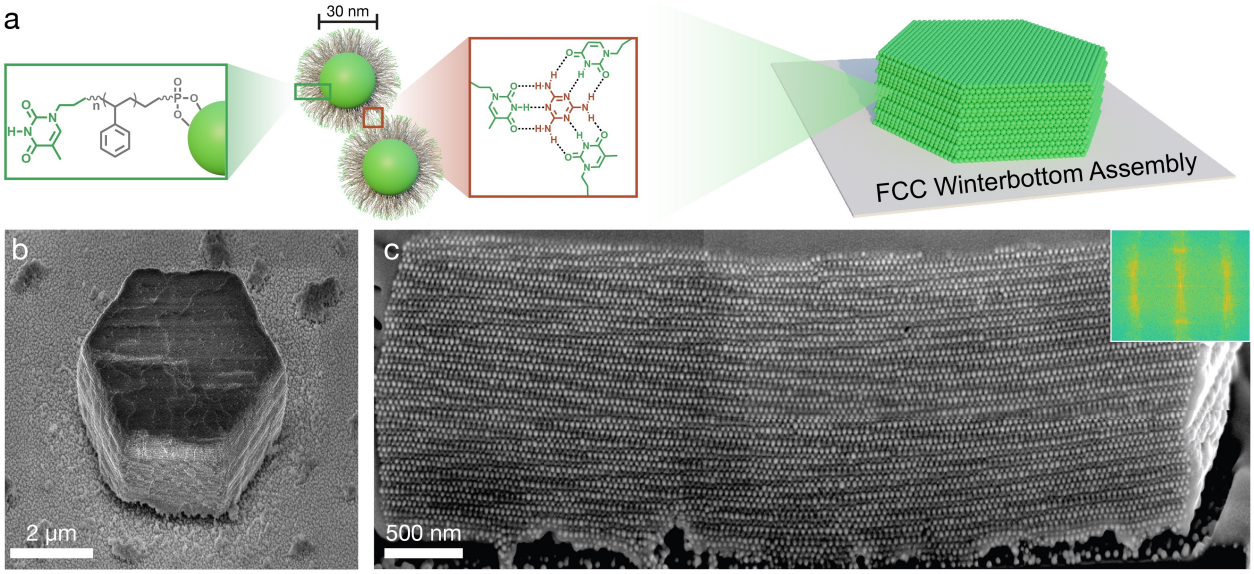


Figure 1: Assembly of nanocomposite tectons and as-formed characterization. a) NCTs are polymer-brush-coated nanoparticles with supramolecular recognition groups at their chain ends. Melamine (brown) is used to mediate the association of thymine (green) functionalized NCTs to form FCC Winterbottom assemblies from gold nanoparticles. b) SEM image of an FCC Winterbottom on a Si substrate containing $\sim 10^6$ nanoparticles. c) Cross-section of the Winterbottom assembly shows close-packing of the NCTs which is expected for an FCC crystal structure. Inset shows the FFT pattern taken from the cross-section image.

To determine the mechanical properties of the as-prepared WB NCTs,we conducted uni-axial compression experiments using an displacement-controlled nanoindenter (Alemnis AG)

at a quasi-static strain rate of $10^{-3}$ $s^{-1}$, providing force-displacement measurements that resulted in the stress-strain relations depicted in Fig. 2a. We performed systematic experiments on different samples to terminal compression strains of $\varepsilon = 20\%$, 30%, and 45% (on as-synthesized samples that were not FIB-milled). As shown, the stress-strain plots are characterized by an initially elastic region followed by the onset of nonlinearity at ∼10% strain, while initial nonlinearity at strains $\varepsilon < 2\%$ results from inevitable minor misalignments between the NCT surface and the compression tip. The effective Young's modulus of the samples, determined from the slope of linear loading regime, was determined to be black $E^* = 1.49 \pm 0.15$ GPa. This effective stiffness of NCT assemblies, similar to that of other NPSLs bonded by non-covalent interactions, is comparable to that of glassy polymers[35] which suggests that the mechanical properties of the NCTs are dominated by the interactions between the polymer brushes. These compression experiments also allowed us to obtain the effective yield strength of our NPSL assemblies, determined to be black $\sigma_y^* = 88 \pm 21$ MPa via the 0.2% offset method, which is rarely reported in NPSL literature since this metric cannot be directly obtained using classical nanoindentation.

Since the compression experiments were conducted *in situ*, this enabled observation of the NCT assemblies' deformation behavior (purpleSupporting Information Video S1). Images of the compression sequence at $\varepsilon = 10\%$, 25%, and 42%, as shown in Figs. 2b, 2c, and 2d, respectively, highlight the behavior of the WB NCTs under different deformation regimes. At $\varepsilon = 10\%$, no significant inelastic deformation was observed, consistent with the primarily linear-elastic regime observed to span beyond this strain measure for all the WB NCTs that were compressed. At $\varepsilon = 25\%$, we observed a noticeable increase in the cross-sectional areas of the WB NCTs, indicating deformation in a plastic flow regime. Finally, at $\varepsilon = 42\%$, vertically aligned cracks emerged on the lateral surfaces of the WB constructions, indicating contributions of a fracture mechanism at large strains.

To characterize the type of permanent deformation that accumulated in the WB NCTs, we performed post-mortem characterization by exposing cross-sections via FIB milling. As

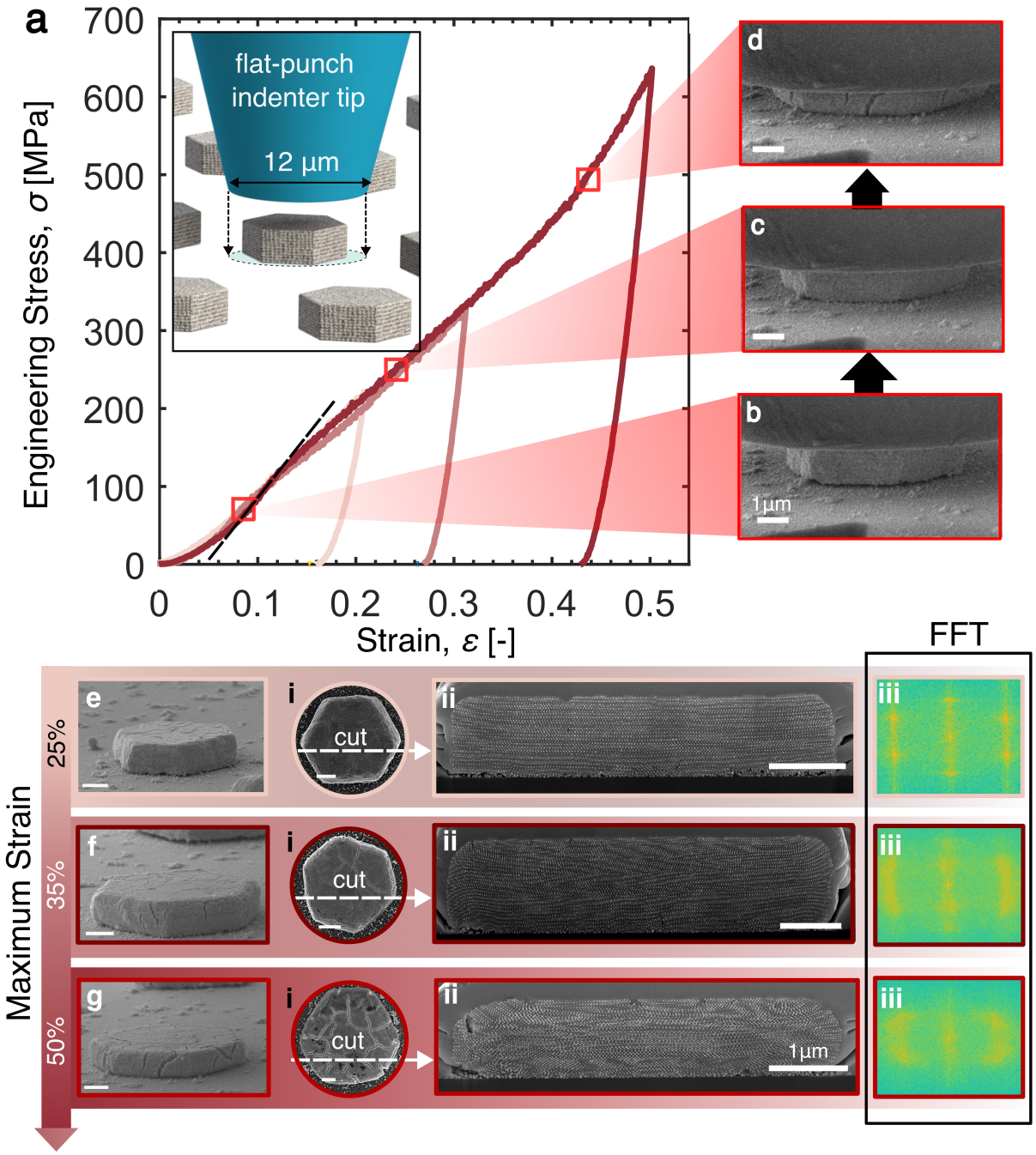


Figure 2: Large-strain *in situ* uniaxial compression of WB NCTs. (a) Stress-Strain plot of three representative WB NCT structures, with insets showing a schematic of the compression procedure. (b,c,d) SEM snapshots of the compression sequence for the sample compressed to 50% strain at 10%, 25%, and 42% strain, respectively. Post-compression images, top view (i), Cross-section view (ii), and FFT of internal structure (iii) after compression to (e) 25%,(f) 35% and (g) 50% strain, respectively.

depicted by the SEM cross-section and corresponding FFT for a sample compressed to 25% strain (Fig. 2e), indications of nanoparticle disorder and permanent deformation begin to become evident in this compressed state. However, examination of their cross-sections obtained via FIB milling after compression, revealed that the nanoparticle ordering was still mostly preserved, as confirmed by their 2D FFT patterns. At a higher strain of 35% (Fig. 2f), emergence of surface cracks was observed, along with a marked loss of long-range internal order which translated to further blurring of the arcs in the FFT pattern. We also observe a shortening in the vertical direction and a widening in the horizontal direction of the pattern in the FFT indicating flow and permanent deformation of the crystal lattice (Supporting Information (Fig. S5). Finally, for the samples subjected to 50% strain (Fig. 2g), we observed significant crack formation and a extensive loss of order in the nanoparticle arrangement. These results suggest that our self-assembled WB NCTs exhibit elasto-plastic behavior, with plastic flow being accommodated by nanoparticle disorder followed by fracture events along nanoparticle facets. As the particles move closer together, enabled by the compliance of polymer brushes, a state of densification was reached, denoted by an increase in slope at the $\varepsilon \approx 40\%$ range likely due to interparticle contact. black While information about the homogeneous deformation could be obtained from the FFTs of the SEM images, slip/failure mechanisms could not be characterized due to the limitations in our microscopy resolution and thus would warrant further studies.

Once we determined the baseline mechanical properties of the as-formed WB NCTs, we proceeded to quantify the effect of FIB milling on the mechanical response of NCTs, since this technique is an established tool for nanofabrication that has been demonstrated specifically to shape NPSLs into functional devices.[32–34] To demonstrate the utility of FIB-milling in shaping our NCTs, we used it to shape our materials into a variety of structures as shown in Fig. 3a. Importantly, we observed no loss in nanoparticle ordering, demonstrating that complex structures retain this necessary key characteristic for NCT-based devices.

We selected the FIB-milled square NCT shape (Fig. 3a i) for subsequent *in situ* mechani-

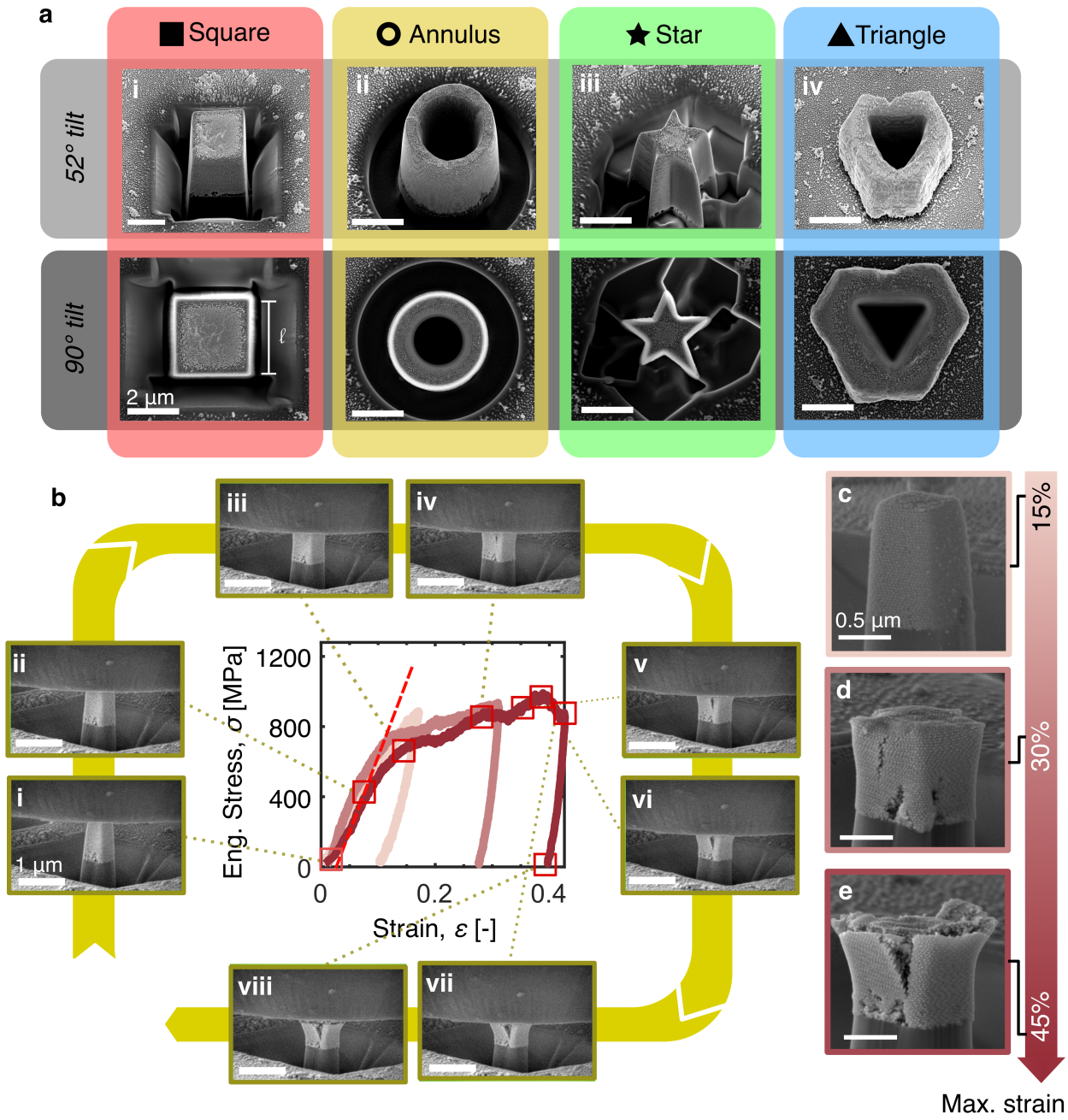


Figure 3: (a) Top view and 52° incline view of (i) square-, (ii) annulus-, (iii) star-, and (iv) triangle-shaped NCTs obtained by FIB. (b) Compression of NCT pillars to 15%, 30% and 45% strain respectively. (i-viii) Snapshots of compression sequence at different strains for the 45% strain compression. Post-compression image of pillar subjected to a maximum strain of (c) 15%, (d) 30% and (e) 45% strain.

cal testing, and fabricated pillars out of the WB NCTs with lateral dimensions ranging from $l \approx 300$ nm to 1 µm and heights of ∼2 µm. Using the same compression protocols as with the WB structures, we compressed these pillars (purpleSupporting Information Video S2) to varying degrees of ultimate deformation, including $\varepsilon = 15\%$, 30%, and 45%, as shown in Fig. 3b. The stress-strain responses of these pillars evidenced a significantly different response from their parent WB NCT structures (Fig. 2a); namely, the pillars exhibited a more defined yield point followed by an increasing flow stress to a level at which fracture in the lateral pillar surfaces took place. The effective stiffness of these pillars was determined to be up to an order of magnitude larger than that of WB NCTs and to vary as a function of the pillar aspect ratio, spanning a range from black $E^* = 4.9$ to 16.9 GPa, corresponding to pillars with lateral dimensions of $l \approx 1.1$ µm and 320 nm, respectively. Similarly, the yield strength of these pillars was higher than that of the WB NCTs, ranging from black $\sigma_y^* = 69.2$ to 426.3 MPa, in some cases up to seven times higher than that of the parent WB structures.

The deformation behavior of these pillars during compression also differed significantly, with yielding and crack formation occurring at $\varepsilon = 10\%$ (Fig. 3b iii) and 25% (Fig. 3b iv), respectively, approximately 10% strain lower than in WB NCTs. At higher strains, the pillars started to petal, i.e., the external surface layer bent away from the bulk while the internal domain continued to plastically flow as observed in the parent WB NCTs (Fig. 3b v-viii).

We hypothesized that the strengthening behavior in the pillars compared to the as-assembled WB NCTs stemmed from a surface-stiffening effect caused by the interaction of the ion beam with the polymer brush matrix, as previous studies have demonstrated that FIB high-energy ions can strengthen polymers by inducing crosslinking.[56–58] black While the precise mechanism of ion-induced crosslinking of polystyrene is complex,[59,60] it is likely that ion irradiation caused chain scission of the polystyrene, and consequently the formation of radicals. These radicals then induced crosslinking via the formation of new bonds between

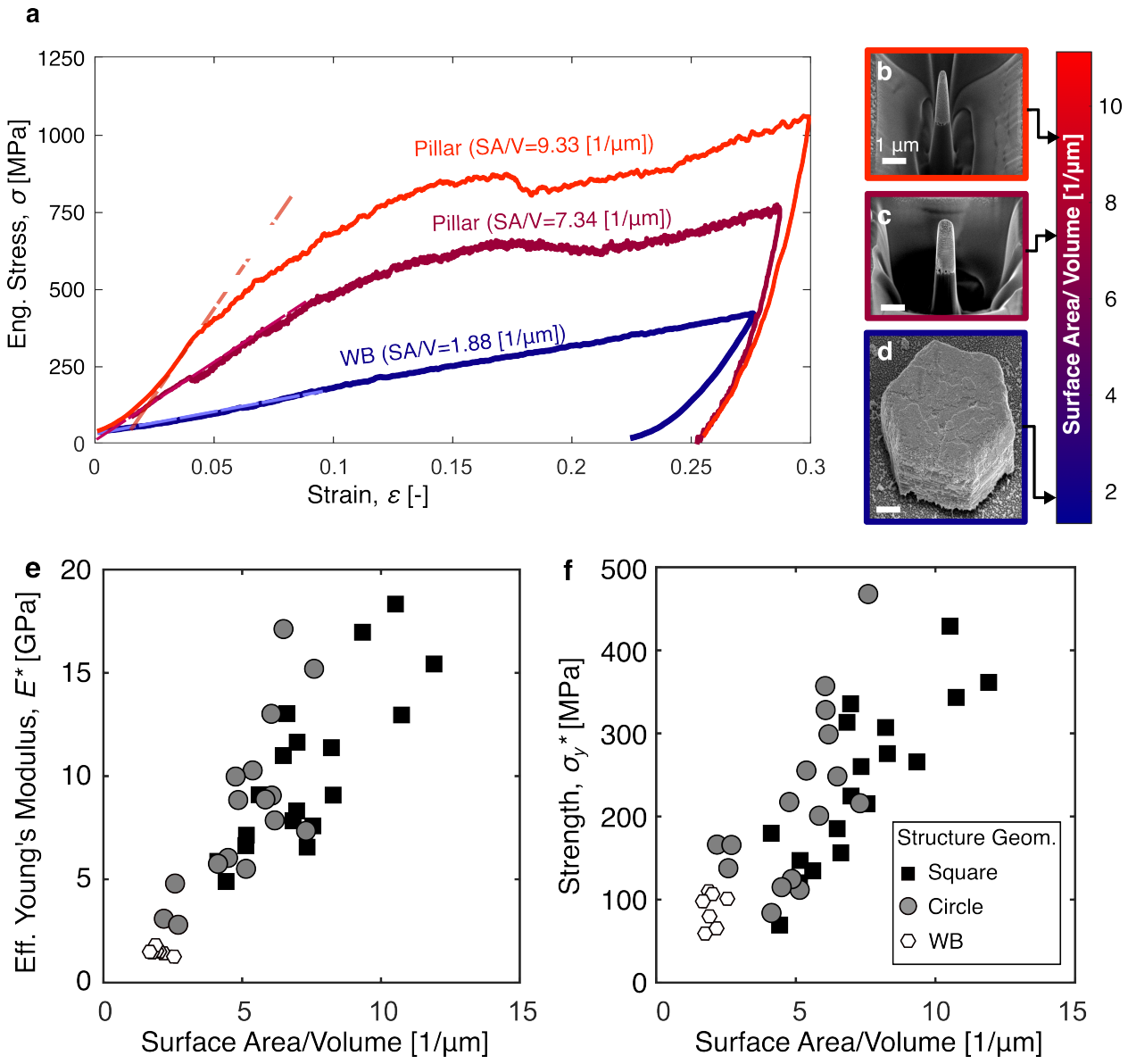


Figure 4: (a) Stress-strain plots for Winterbottom, and two circular pillars (images shown in (b), (c), and (d) respectively). Variation of (e) stiffness and (f) strength with surface-area-to-volume ratio for square pillars (square), circular pillars (circle) and winterbottoms (hexagon)(error bars lie within data points).

neighboring polymer chains,[61] resulting in the stiffening of the polymer. This mechanism of stiffening would be consistent with the observation that the aspect ratio of the pillars had a significant influence on their mechanical properties, as the high-energy ions would only be expected to react with the outermost portions of the FIB-milled material. To test this hypothesis, square pillars with systematically varying surface-area-to-volume (SA/V) ratios were fabricated; compression of these pillars showed that they did indeed exhibit varying degrees of stiffening and strengthening (Fig. 4a).

This surface effect can be clearly visualized when plotting the stiffness and strength of all the milled pillars against their SA/V ratios (Fig. 4e,f). Increasing the SA/V ratio led to a quasi-linear increase in the strength and stiffness black (slope of 1.57 GPa $\mu$m) of the milled NCTs, explaining the size-dependent stiffnesses and strengths of the milled pillars. Additionally, experiments of square and circular pillars (purpleSupporting Information Video S3) at comparable SA/V ratios demonstrated that the shape of the pillars had minimal effect on their mechanical properties (Fig. 4b,c).

To determine if the surface stiffening effect originated from the crosslinking of the polymer brushes on the NCTs, we prepared a polymer film using the same polymer feedstock used to form the polymer brushes on the NCTs (14kDa Thy-functionalized polystyrene) and used a FIB to mill pillars out of this film. *In situ* compression of these polymer pillars showed a similar strengthening effect, where increasing their SA/V ratio led to a similar increase in their mechanical properties (Fig. S8), further supporting our hypothesis that the strengthening of the NCT pillars arose due to crosslinking of the polymer brushes on the surface of the NCTs.

The ability to use a FIB to tune the mechanical properties of the NCT assemblies has the potential to vastly expand their end-use cases. Since each application requires a particular set of mechanical properties, understanding how shaping these materials via FIB milling leads to variable properties is crucial to precisely engineer NCT-containing devices. To that end, we developed two models—one analytical and one computational—that allow us to predict the

mechanical response of arbitrary NCT assemblies. First, we developed a core-shell model that provides an analytical relation between the stiffnesses of our milled pillars and their SA/V ratios, which assumes that the surface-particle domain has a higher stiffness than the core-particle domain. The radius (or hydrodynamic radius for non-circular cross-sections) and height of the pillar are taken as $r$ and $h$, respectively, with the thickness of the surface represented by $t$. Taking the core-particle domain to have a modulus $E$ (which is obtained from our experiments on the as-formed WB NCTs) and the surface-particle domain to have a modulus $E_s$, the effective modulus $E_{eff}$ of a core-shell structure can be represented as black

$$E_{eff} = \frac{E + (E_s - E)(\alpha t - 2\beta)}{1 + \beta\left(\frac{E}{E_s} - 1\right)}. \tag{1}$$

Here, $\alpha$ denotes the SA/V ratio and $\beta = t/h$ is the ratio of the surface-layer thickness to the height of the pillar (details in the Supporting Information). This expression presents a linear relation between the effective stiffness and the surface-area-to-volume ratio, consistent with our experiments (Fig. 4b,c).

Further, black we use multivariate optimization to obtain the values of $E_s$ and $t$ that result in the best fit (least-squares sense) to our experiments, namely 44.77 GPa and 36.4 nm, respectively (details in Supporting Information). Using this stiffness value for the surface domain, our model (Eq. 1) predicted the effective stiffness of our samples, as shown in Fig. 5a.

This core-shell model can be used to predict the stiffness of the surface particles and is effective to determine the stiffness of pillars of other aspect ratios. Given its simplicity, however, we restrict its use to the purely linear regime, prior to the onset of nonlinearity emerging from plastic flow of nanoparticles.

To overcome this limitation of predicting the response of NCTs beyond the linear regime, our second model consisted of a discrete element method (DEM) model, where each numerical particle represented the gold nanoparticles in the NCTs. The particles are connected to one another with bonds that represent the polymer brushes in our system. Bonds effectively

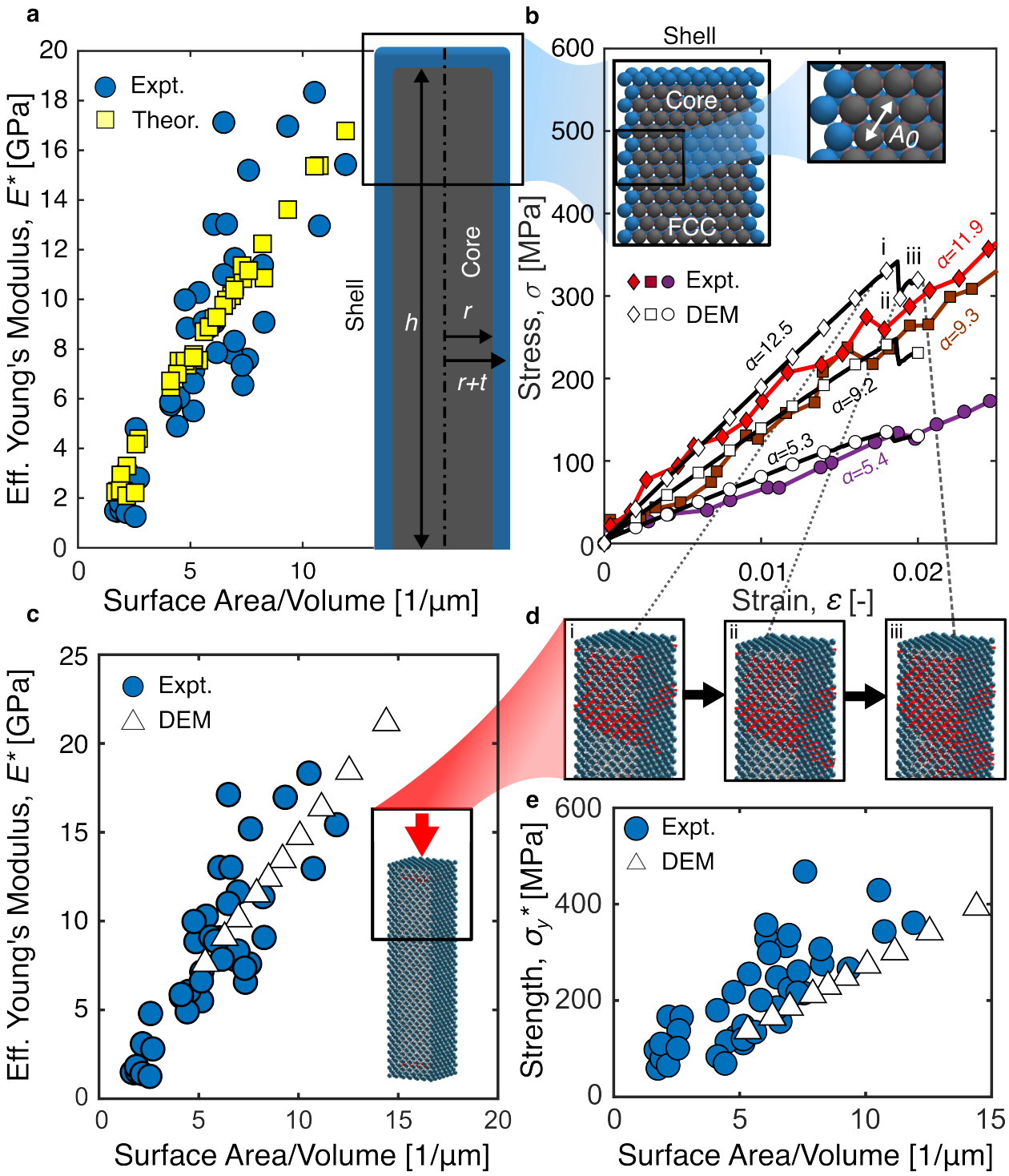


Figure 5: Analytical and numerical tools for predicting the effective stiffness of NCT samples. (a) Stiffness vs. surface-area-to-volume ratio as obtained from the theoretical core-shell model and experiments, with a schematic of core-shell model definitions. (b) Stress vs. strain responses obtained from DEM (red) and experiments (blue). Plots of (c) stiffness and (e) strength vs surface-area-to-volume ratio obtained through DEM (red) and experiments (blue). (d)(i,ii,iii) Snapshots of DEM simulations with progressive compression and failure.

act like beams providing resisting force and moment to relative motion and rotation of neighboring particles. Upon a selected failure criterion, bonds will break and provide no further force and moment to the system. As shown in Fig. 5b, the particles are initially arranged in an FCC structure with an inter-particle spacing defined as $A_0 \approx 35 \pm 5$ nm obtained from FFT analysis on the WB NCTs. To accurately capture any defects present in our structure, Gaussian noise corresponding to the standard deviation in particle placement is included.

To capture the surface stiffening effect, bonds are modeled with two stiffnesses, the surface-domain elastic stiffness and the bulk-domain elastic stiffness, depending on the location of the particles. The structure, comprised of 500 particles, is then subjected to uniaxial compression applied as a prescribed displacement along the $Z$-axis with periodic boundary conditions. The bulk-domain elastic stiffness of the bonds is tuned such that the elastic modulus obtained from the simulation matches the stiffness of the WB NCTs. Next, to capture size effects, we generated pillars of different SA/V ratios and subject them to uniaxial compression with free lateral boundary conditions. The surface-domain elastic stiffnesses are then tuned such that the elastic modulus for pillars of different SA/V ratios matches the stiffness obtained from compression of the NCT pillars for similar SA/V values. To capture the non-linear behaviour up to yield of the NCTs, these bonds are modeled to have a threshold stress beyond which they fail. The strength of the inter-particle bonds in the bulk-domain were obtained by matching the strength of the periodic-boundary-condition DEM simulation to that of the bulk NCT samples. Due to surface stiffening effects, the bulk-domain bonds break first at the yield point of the NCTs. Hence, the bond strength of the surface particles presumably have little effect on NCT yielding and are assumed to preserve the same stiffening ratio of surface-domain bond stiffness to bulk-domain bond stiffness. With the tuned bond behavior, the stress-strain responses from the DEM simulations present a close match to our experiments for samples of similar surface-area-to-volume ratio (Fig. 5c,d). Furthermore, on comparing the strength and stiffness obtained from the DEM

simulations to those obtained experimentally, we see a similar trend for both indicating that the model is able to predict the properties of the FIB-strengthened NCT pillars (Fig. 5e).

In conclusion, we have herein demonstrated that FIB-milling can be used to both shape self-assembled NCT NPSLs and tune their mechanical properties. Our experiments revealed that FIB-milling results in a surface stiffening effect, which can be exploited as a mechanism to tune the mechanical properties of these NCT NPSLs via their surface-area-to-volume ratios. We also developed an analytical core-shell model and a DEM representation that can be used to efficiently predict the mechanical properties of these NPSLs, paving the way towards the design of 3D NCT architectures with user-defined mechanical properties. Given that the mesoscale architecture of NPSL-based materials plays an important role in dictating their material properties,[62–64] the ability to use the FIB to precisely shape them and go beyond their thermodynamically-defined shapes could represent a step forward in allowing NPSLs to be used in a wider range of applications. In addition, the fundamental mechanical insight developed in this study will be necessary for the processing and application of these NPSL-based materials. Further explorations on the effect of crystal symmetry, particle size, polymer brush composition, and interparticle interactions on their mechanical behavior will advance our understanding and control of NPSL-based materials, and potentially make NPSL materials one of the most versatile nano-architected material systems reported to date.

# Acknowledgement

C.M.P. and S.D. acknowledge the support from the National Science Foundation (NSF) through CAREER Award CMMI-2142460. R.J.M acknowledges support in part by the U.S. Army Research Office under Grant W911NF-18-1-0197, NSF CAREER Award CHE-1653289, and the Department of the Navy, Office of Naval Research, under ONR award number N00014-22-1-2148. J.E.A. and Z.Z. acknowledge the support from the NSF under award number CMMI-2033779. The authors thank Margaret Lee for support in sample

preparation, Rebecca Li and Carl Thrasher for sample characterization at Argonne National Laboratory, and Theodore Hueckel for helpful discussions.

# Supporting Information Available

Materials, instrumentation, material synthesis and characterization, FFT analysis of lattice order, geometric analysis of pillars, mechanical analysis of pillars, compression of polystyrene pillars, core-shell model derivation, DEM algorithm, and supplementary figures.

## Videos

- `SIVideo1_WB_30pStrain_x20.mp4`: *In situ* uniaxial compression of an as-assembled NCT Winterbottom construction to $\varepsilon = 30\%$, sample width in SEM image 5.95 µm, playback speed $\times 20$.
- `SIVideo2_SqPillar_30pStrain_x20.mp4`: *In situ* uniaxial compression of FIB-milled NCT square pillar to $\varepsilon = 30\%$, sample width in SEM image $\sim$1 µm, playback speed $\times 20$.
- `SIVideo3_CircPillar_44pStrain_x20.mp4`: *In situ* uniaxial compression of FIB-milled NCT circular pillar to $\varepsilon = 44\%$, sample diameter in SEM image 1.2 µm, playback speed $\times 20$.

# References

(1) Lee, M. S.; Yee, D. W.; Ye, M.; Macfarlane, R. J. Nanoparticle Assembly as a Materials Development Tool. *Journal of the American Chemical Society* **2022**, *144*, 3330–3346.

(2) Schulz, F.; Pavelka, O.; Lehmkühler, F.; Westermeier, F.; Okamura, Y.; Mueller, N. S.;

Reich, S.; Lange, H. Structural order in plasmonic superlattices. *Nature communications* **2020**, *11*, 1–9.

(3) Santos, P. J.; Gabrys, P. A.; Zornberg, L. Z.; Lee, M. S.; Macfarlane, R. J. Macroscopic materials assembled from nanoparticle superlattices. *Nature* **2021**, *591*, 586–591.

(4) Bodelón, G.; Montes-García, V.; López-Puente, V.; Hill, E. H.; Hamon, C.; Sanz-Ortiz, M. N.; Rodal-Cedeira, S.; Costas, C.; Celiksoy, S.; Pérez-Juste, I., et al. Detection and imaging of quorum sensing in Pseudomonas aeruginosa biofilm communities by surface-enhanced resonance Raman scattering. *Nature materials* **2016**, *15*, 1203–1211.

(5) Park, D. J.; Zhang, C.; Ku, J. C.; Zhou, Y.; Schatz, G. C.; Mirkin, C. A. Plasmonic photonic crystals realized through DNA-programmable assembly. *Proceedings of the National Academy of Sciences* **2015**, *112*, 977–981.

(6) Sun, L.; Lin, H.; Kohlstedt, K. L.; Schatz, G. C.; Mirkin, C. A. Design principles for photonic crystals based on plasmonic nanoparticle superlattices. *Proceedings of the National Academy of Sciences* **2018**, *115*, 7242–7247.

(7) Cai, Z.; Li, Z.; Ravaine, S.; He, M.; Song, Y.; Yin, Y.; Zheng, H.; Teng, J.; Zhang, A. From colloidal particles to photonic crystals: advances in self-assembly and their emerging applications. *Chemical Society Reviews* **2021**, *50*, 5898–5951.

(8) Yamamoto, K.; Majetich, S. A.; McCartney, M. R.; Sachan, M.; Yamamuro, S.; Hirayama, T. Direct visualization of dipolar ferromagnetic domain structures in Co nanoparticle monolayers by electron holography. *Applied Physics Letters* **2008**, *93*, 082502.

(9) Lisiecki, I.; Parker, D.; Salzemann, C.; Pileni, M. Face-centered cubic supra-crystals and disordered three-dimensional assemblies of 7.5 nm cobalt nanocrystals: Influence of the mesoscopic ordering on the magnetic properties. *Chemistry of materials* **2007**, *19*, 4030–4036.

(10) Li, J.; Wang, Y.; Zhou, T.; Zhang, H.; Sun, X.; Tang, J.; Zhang, L.; Al-Enizi, A. M.; Yang, Z.; Zheng, G. Nanoparticle superlattices as efficient bifunctional electrocatalysts for water splitting. *Journal of the American Chemical Society* **2015**, *137*, 14305–14312.

(11) Kang, Y.; Ye, X.; Chen, J.; Qi, L.; Diaz, R. E.; Doan-Nguyen, V.; Xing, G.; Kagan, C. R.; Li, J.; Gorte, R. J., et al. Engineering catalytic contacts and thermal stability: gold/iron oxide binary nanocrystal superlattices for CO oxidation. *Journal of the American Chemical Society* **2013**, *135*, 1499–1505.

(12) Bauer, J.; Meza, L. R.; Schaedler, T. A.; Schwaiger, R.; Zheng, X.; Valdevit, L. Nanolattices: An Emerging Class of Mechanical Metamaterials. *Advanced Materials* **2017**, *29*, 1–26.

(13) Begley, M. R.; Gianola, D. S.; Ray, T. R. Bridging functional nanocomposites to robust macroscale devices. *Science* **2019**, *364*, eaav4299.

(14) Cheng, Z.; Jones, M. R. Assembly of planar chiral superlattices from achiral building blocks. *Nature communications* **2022**, *13*, 1–11.

(15) Gabrys, P. A.; Macfarlane, R. J. Controlling crystal texture in programmable atom equivalent thin films. *ACS nano* **2019**, *13*, 8452–8460.

(16) Shevchenko, E. V.; Talapin, D. V.; Kotov, N. A.; O'Brien, S.; Murray, C. B. Structural diversity in binary nanoparticle superlattices. *Nature* **2006**, *439*, 55–59.

(17) Talapin, D. V.; Shevchenko, E. V.; Bodnarchuk, M. I.; Ye, X.; Chen, J.; Murray, C. B. Quasicrystalline order in self-assembled binary nanoparticle superlattices. *Nature* **2009**, *461*, 964–967.

(18) Shevchenko, E. V.; Talapin, D. V.; Murray, C. B.; O'Brien, S. Structural characterization of self-assembled multifunctional binary nanoparticle superlattices. *Journal of the American Chemical Society* **2006**, *128*, 3620–3637.

(19) Auyeung, E.; Li, T. I.; Senesi, A. J.; Schmucker, A. L.; Pals, B. C.; de La Cruz, M. O.; Mirkin, C. A. DNA-mediated nanoparticle crystallization into Wulff polyhedra. *Nature* **2014**, *505*, 73–77.

(20) Auyeung, E.; Macfarlane, R. J.; Choi, C. H. J.; Cutler, J. I.; Mirkin, C. A. Transitioning DNA-Engineered Nanoparticle Superlattices from Solution to the Solid State. *Advanced Materials* **2012**, *24*, 5181–5186.

(21) Yarema, M.; Kovalenko, M. V.; Hesser, G.; Talapin, D. V.; Heiss, W. Highly monodisperse bismuth nanoparticles and their three-dimensional superlattices. *Journal of the American Chemical Society* **2010**, *132*, 15158–15159.

(22) Ni, B.; Gonzalez-Rubio, G.; Cölfen, H. Self-Assembly of Colloidal Nanocrystals into 3D Binary Mesocrystals. *Accounts of Chemical Research* **2022**, e202112461–9130.

(23) Lewis, D. J.; Zornberg, L. Z.; Carter, D. J.; Macfarlane, R. J. Single-crystal Winterbottom constructions of nanoparticle superlattices. *Nature materials* **2020**, *19*, 719–724.

(24) Kim, J.; Dey, J.; Umar, A.; Ha, J.-M.; Lee, S.-J.; Kim, J.; Choi, S.-M. Highly Stable Nanoparticle Supercrystals Formed by the Aldol Reaction in Conjunction with Slow Solvent Evaporation. *Chemistry of Materials* **2022**, *34*, 6744–6752.

(25) Domènech, B.; Tan, A. T.; Jelitto, H.; Zegarra Berodt, E.; Blankenburg, M.; Focke, O.; Cann, J.; Cem Tasan, C.; Colombi Ciacchi, L.; Müller, M., et al. Strong Macroscale Supercrystalline Structures by 3D Printing Combined with Self-Assembly of Ceramic Functionalized Nanoparticles. *Advanced engineering materials* **2020**, *22*, 2000352.

(26) Cheng, W.; Park, N.; Walter, M. T.; Hartman, M. R.; Luo, D. Nanopatterning self-assembled nanoparticle superlattices by moulding microdroplets. *Nature Nanotechnology* **2008**, *3*, 682–690.

(27) Santhanam, V.; Andres, R. P. Microcontact printing of uniform nanoparticle arrays. *Nano Letters* **2004**, *4*, 41–44.

(28) Chiang, N.; Scarabelli, L.; Vinnacombe-Willson, G. A.; Pérez, L. A.; Dore, C.; Mihi, A.; Jonas, S. J.; Weiss, P. S. Large-Scale Soft-Lithographic Patterning of Plasmonic Nanoparticles. *ACS materials letters* **2021**, *3*, 282–289.

(29) Jiang, C.; Oshima, D.; Iwata, S.; Pong, P. W.; Kato, T. Patterned arrays of assembled nanoparticles prepared by interfacial assembly and femtosecond laser fabrication. *Journal of Nanoparticle Research* **2020**, *22*, 1–12.

(30) Langford, R. M.; Nellen, P. M.; Gierak, J.; Fu, Y. Focused ion beam micro-and nanoengineering. *MRS bulletin* **2007**, *32*, 417–423.

(31) Li, P.; Chen, S.; Dai, H.; Yang, Z.; Chen, Z.; Wang, Y.; Chen, Y.; Peng, W.; Shan, W.; Duan, H. Recent advances in focused ion beam nanofabrication for nanostructures and devices: Fundamentals and applications. *Nanoscale* **2021**, *13*, 1529–1565.

(32) Si, K. J.; Sikdar, D.; Chen, Y.; Eftekhari, F.; Xu, Z.; Tang, Y.; Xiong, W.; Guo, P.; Zhang, S.; Lu, Y., et al. Giant plasmene nanosheets, nanoribbons, and origami. *ACS nano* **2014**, *8*, 11086–11093.

(33) Si, K. J.; Dong, D.; Shi, Q.; Zhu, W.; Premaratne, M.; Cheng, W. Ultrathin fresnel lens based on plasmene nanosheets. *Materials Today* **2019**, *23*, 9–15.

(34) Okuda, M.; Schwarze, T.; Eloi, J.-C.; Jones, S. W.; Heard, P. J.; Sarua, A.; Ahmad, E.; Kruglyak, V. V.; Grundler, D.; Schwarzacher, W. Top-down design of magnonic crystals from bottom-up magnetic nanoparticles through protein arrays. *Nanotechnology* **2017**, *28*, 155301.

(35) Gu, X. W. Mechanical properties of architected nanomaterials made from organic–inorganic nanocrystals. *JOM* **2018**, *70*, 2205–2217.

(36) Tam, E.; Podsiadlo, P.; Shevchenko, E.; Ogletree, D. F.; Delplancke-Ogletree, M.-P.; Ashby, P. D. Mechanical Properties of Face-Centered Cubic Supercrystals of Nanocrystals. *Nano Letters* **2010**, *10*, 2363–2367, PMID: 20515036.

(37) Podsiadlo, P.; Krylova, G.; Lee, B.; Critchley, K.; Gosztola, D. J.; Talapin, D. V.; Ashby, P. D.; Shevchenko, E. V. The Role of Order, Nanocrystal Size, and Capping Ligands in the Collective Mechanical Response of Three-Dimensional Nanocrystal Solids. *Journal of the American Chemical Society* **2010**, *132*, 8953–8960, PMID: 20550200.

(38) Choi, J.; Hui, C. M.; Pietrasik, J.; Dong, H.; Matyjaszewski, K.; Bockstaller, M. R. Toughening fragile matter: mechanical properties of particle solids assembled from polymer-grafted hybrid particles synthesized by ATRP. *Soft Matter* **2012**, *8*, 4072–4082.

(39) Dreyer, A.; Feld, A.; Kornowski, A.; Yilmaz, E. D.; Noei, H.; Meyer, A.; Krekeler, T.; Jiao, C.; Stierle, A.; Abetz, V., et al. Organically linked iron oxide nanoparticle supercrystals with exceptional isotropic mechanical properties. *Nature materials* **2016**, *15*, 522–528.

(40) Bor, B.; Giuntini, D.; Domènech, B.; Plunkett, A.; Kampferbeck, M.; Vossmeyer, T.; Weller, H.; Scheider, I.; Schneider, G. A. Constitutive and fracture behavior of ultrastrong supercrystalline nanocomposites. *Applied Physics Reviews* **2021**, *8*, 031414.

(41) Plunkett, A.; Kampferbeck, M.; Bor, B.; Sazama, U.; Krekeler, T.; Bekaert, L.; Noei, H.; Giuntini, D.; Fröba, M.; Stierle, A., et al. Strengthening Engineered Nanocrystal Three-Dimensional Superlattices via Ligand Conformation and Reactivity. *ACS nano* **2022**, *16*, 11692–11707.

(42) Giuntini, D.; Zhao, S.; Krekeler, T.; Li, M.; Blankenburg, M.; Bor, B.; Schaan, G.; Domènech, B.; Müller, M.; Scheider, I., et al. Defects and plasticity in ultrastrong supercrystalline nanocomposites. *Science advances* **2021**, *7*, eabb6063.

(43) Wang, Z.; Christodoulides, A. D.; Dai, L.; Zhou, Y.; Dai, R.; Xu, Y.; Nian, Q.; Wang, J.; Malen, J. A.; Wang, R. Y. Nanocrystal Ordering Enhances Thermal Transport and Mechanics in Single-Domain Colloidal Nanocrystal Superlattices. *Nano Letters* **2022**, *22*, 4669–4676, PMID: 35639612.

(44) Lewis, D. J.; Carter, D. J.; Macfarlane, R. J. Using DNA to Control the Mechanical Response of Nanoparticle Superlattices. *Journal of the American Chemical Society* **2020**, *142*, 19181–19188.

(45) Mueggenburg, K. E.; Lin, X.-M.; Goldsmith, R. H.; Jaeger, H. M. Elastic membranes of close-packed nanoparticle arrays. *Nature materials* **2007**, *6*, 656–660.

(46) Wang, J.; Schwenger, J.; Ströbel, A.; Feldner, P.; Herre, P.; Romeis, S.; Peukert, W.; Merle, B.; Vogel, N. Mechanics of colloidal supraparticles under compression. *Science Advances* **2021**, *7*, eabj0954.

(47) Giuntini, D.; Davydok, A.; Blankenburg, M.; Domènech, B.; Bor, B.; Li, M.; Scheider, I.; Krywka, C.; Müller, M.; Schneider, G. A. Deformation behavior of cross-linked supercrystalline nanocomposites: an in situ SAXS/WAXS study during uniaxial compression. *Nano letters* **2021**, *21*, 2891–2897.

(48) Winterbottom, W. L. Equilibrium shape of a small particle in contact with a foreign substrate. *Acta Metallurgica* **1967**, *15*, 303–310.

(49) Marks, L.; Peng, L. Nanoparticle shape, thermodynamics and kinetics. *Journal of Physics: Condensed Matter* **2016**, *28*, 053001.

(50) Sun, L.; Lin, H.; Li, Y.; Zhou, W.; Du, J. S.; Mirkin, C. A. Position-and Orientation-Controlled Growth of Wulff-Shaped Colloidal Crystals Engineered with DNA. *Advanced Materials* **2020**, *32*, 2005316.

(51) Santos, P. J.; Cheung, T. C.; Macfarlane, R. J. Assembling ordered crystals with disperse building blocks. *Nano letters* **2019**, *19*, 5774–5780.

(52) Santos, P. J.; Macfarlane, R. J. Reinforcing supramolecular bonding with magnetic dipole interactions to assemble dynamic nanoparticle superlattices. *Journal of the American Chemical Society* **2020**, *142*, 1170–1174.

(53) Zhang, J.; Santos, P. J.; Gabrys, P. A.; Lee, S.; Liu, C.; Macfarlane, R. J. Self-assembling nanocomposite tectons. *Journal of the American Chemical Society* **2016**, *138*, 16228–16231.

(54) Lee, M. S.; Alexander-Katz, A.; Macfarlane, R. J. Nanoparticle Assembly in High Polymer Concentration Solutions Increases Superlattice Stability. *Small* **2021**, *17*, 2102107.

(55) Yee, D. W.; Lee, M. S.; An, J.; Macfarlane, R. J. Reversible Diffusionless Phase Transitions in 3D Nanoparticle Superlattices. *Journal of the American Chemical Society* **2023**, *145*, 6051–6056, PMID: 36898204.

(56) Samira, R.; Vakahi, A.; Eliasy, R.; Sherman, D.; Lachman, N. Mechanical and compositional implications of gallium ion milling on epoxy resin. *Polymers* **2021**, *13*, 2640.

(57) Velez, N. R.; Allen, F. I.; Jones, M. A.; Donohue, J.; Li, W.; Pister, K.; Govindjee, S.; Meyers, G. F.; Minor, A. M. Nanomechanical testing of freestanding polymer films: in situ tensile testing and T g measurement. *Journal of Materials Research* **2021**, *36*, 2456–2464.

(58) Wang, S.; Yang, Y.; Zhou, L. M.; Mai, Y.-W. Size effect in microcompression of epoxy micropillars. *Journal of materials science* **2012**, *47*, 6047–6055.

(59) Aoki, Y.; Kouchi, N.; Shibata, H.; Tagawa, S.; Tabata, Y.; Imamura, S. Radiation effects of ion beams on polystyrene resist films. *Nuclear Instruments and Methods in*

*Physics Research Section B: Beam Interactions with Materials and Atoms* **1988**, *33*, 799–802.

(60) Seki, S.; Tsukuda, S.; Maeda, K.; Matsui, Y.; Saeki, A.; Tagawa, S. Inhomogeneous distribution of crosslinks in ion tracks in polystyrene and polysilanes. *Phys. Rev. B* **2004**, *70*, 144203.

(61) Velez, N. R.; Allen, F. I.; Jones, M. A.; Donohue, J.; Li, W.; Pister, K.; Govindjee, S.; Meyers, G. F.; Minor, A. M. Nanomechanical testing of freestanding polymer films: in situ tensile testing and Tg measurement. *Journal of Materials Research* **2021**, *36*, 2456–2464.

(62) Zornberg, L. Z.; Lewis, D. J.; Mertiri, A.; Hueckel, T.; Carter, D. J. D.; Macfarlane, R. J. Self-Assembling Systems for Optical Out-of-Plane Coupling Devices. *ACS Nano* **2023**, *17*, 3394–3400, PMID: 36752596.

(63) Ross, M. B.; Ku, J. C.; Vaccarezza, V. M.; Schatz, G. C.; Mirkin, C. A. Nanoscale form dictates mesoscale function in plasmonic DNA–nanoparticle superlattices. *Nature nanotechnology* **2015**, *10*, 453–458.

(64) Kim, S.; Zheng, C. Y.; Schatz, G. C.; Aydin, K.; Kim, K.-H.; Mirkin, C. A. Mie-resonant three-dimensional metacrystals. *Nano letters* **2020**, *20*, 8096–8101.

# TOC Graphic

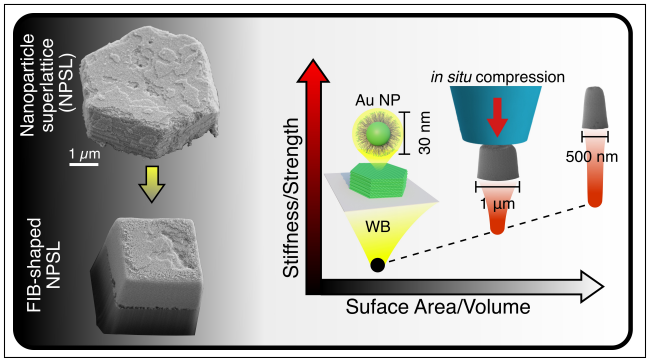
Nanoparticle superlattice (NPSL)
1 μm
FIB-shaped NPSL
Au NP
30 nm
WB
in situ compression
1 μm
500 nm
Stiffness/Strength
Suface Area/Volume